npj computational materials

www.nature.com/npjcompumats

ARTICLE OPEN

Check for updates

Adaptive finite differencing in high accuracy electronic structure calculations

E. L. Briggs[1]✉, Wenchang Lu[1,2]✉ and J. Bernholc[1,2]✉

A multi-order Adaptive Finite Differencing (AFD) method is developed for the kinetic energy operator in real-space, grid-based electronic structure codes. It uses atomic pseudo orbitals produced by the corresponding pseudopotential codes to optimize the standard finite difference (SFD) operators for improved precision. Results are presented for a variety of test systems and Bravais lattice types, including the well-known Δ test for 71 elements in the periodic table, the Mott insulator NiO, and borax decahydrate, which contains covalent, ionic, and hydrogen bonds. The tests show that an 8th-order AFD operator leads to the same average Δ value as that achieved by plane-wave codes and is typically far more accurate and has a much lower computational cost than a 12th-order SFD operator. The scalability of real-space electronic calculations is demonstrated for a 2016-atom NiO cell, for which the computational time decreases nearly linearly when scaled from 18 to 144 CPU-GPU nodes.

npj Computational Materials (2024)10:17 ; https://doi.org/10.1038/s41524-024-01203-y

INTRODUCTION

Density functional theory (DFT)[1–3] has enabled accurate, ab initio predictions of materials properties and explanations of a wide range of experimental data. Tens of thousands of DFT calculations are performed each year. The reliability of DFT predictions has led to materials-genome-type projects[4–7], in which a large set of possible material compositions and structures are screened by DFT calculations in order to identify those with promising properties. Those with the most potential are then suggested or selected for experimental synthesis and evaluation.

Reliability of predictions is critical to any evaluation of potential predictions, and the accuracy of practical DFT calculations is thus a factor when choosing a suitable computational method. However, full-precision DFT calculations can be computationally expensive, especially if complex structures or multi-component systems are involved, and the choice of approach and code often involves a tradeoff between computational accuracy and practicality. Fortunately, the methodology has advanced to the point where the results of several widely-used DFT codes agree well with each other and a set of benchmark high-precision calculations for a large set of elements across the periodic table[8]. However, the tradeoffs remain for more complex systems or large survey studies, requiring practical compromises between the computational expense, accuracy, and even the choice of the computational method. This paper describes a significant advance in the class of methods that use real-space grids to solve DFT equations. By using adaptive finite differencing to discretize the kinetic energy operator, the real-space results agree with those of plane-wave-based codes using much lower grid densities than those previously required and reproducing the benchmark DFT results[8] at the same accuracy level as those of plane-wave-based and all-electron codes. The improved discretization enables high-precision real-space calculations at a substantially reduced cost while leveraging the well-known advantages of real-space methods of easy parallelization across many nodes, including multi-CPU and multi-GPU configurations, and avoiding the use of Fast Fourier Transform algorithms, which require global communication across nodes.

Briefly, in density functional theory, the ground state electronic structure of many-electron systems is solved numerically, typically after introducing the Kohn-Sham equation[2], which is derived variationally from the total energy functional after approximating the kinetic energy by that of non-interacting electrons. The electrons are described as single particles in the presence of an external potential stemming from nuclei and externally applied fields and an effective potential, introduced by interactions with other electrons and the effects of the Pauli exclusion principle and spin:

$$\left[-\nabla^2 + V_{ext}(r) + V_{eff}(r)\right]\psi_i(r) = \varepsilon_i\psi_i(r)\, i = 1, \ldots N \quad (1)$$

for the N electrons in the system. Rydberg atomic units are used throughout. The effective potential is further split into the classical electron-electron repulsion part and the exchange-correlation part that accounts for all effects left out by the classical non-interacting electrons picture. While it has been proven that the exact exchange-correlation potential is only a functional of the total electron density[1], its functional form is unknown. Nevertheless, excellent approximations exist, starting with the local density approximation, which pointwise approximates this potential with that of the uniform-density electron gas through a "Jacobs ladder" of functionals with increasing complexity and a better description of the exchange-correlation energy[9]. Non-local approximations to exchange-correlation functionals have also been devised, including various forms of hybrid functionals[10–12].

Depending on the treatment of the external potential from the nuclei, the methods to solve the Kohn-Sham equation can be categorized into two groups, the first being the all-electron method that includes both core and valence electrons in the calculations[13–15]. The other group replaces the nuclei and inert core electrons with atom-derived pseudopotentials[16–19] or effective core potentials[20–22] that are constructed to accurately describe the interactions of valence electrons with the ionic cores. Pseudopotentials dramatically reduce the numbers of

[1]Department of Physics, North Carolina State University, Raleigh, NC 27695-8202, USA. [2]Computational Sciences & Engineering Division, Oak Ridge National Laboratory, TN 37831 Raleigh, USA. ✉email: elbriggs@ncsu.edu; wlu2@ncsu.edu; bernholc@ncsu.edu

electrons and plane waves or grid points included in the calculations[23]. Furthermore, because the valence electrons experience a softer pseudopotential instead of the real potential, the wave functions are smoother, and the basis set required to describe them is much smaller. Another advantage is the implicit inclusion of relativistic effects in the pseudopotential so that relativistic effects do not need to be explicitly addressed in the numerical solution of the Kohn-Sham equations[24]. For these reasons, most large DFT calculations use pseudopotentials. When pseudopotentials are carefully constructed from atomic all-electron calculations, they are transferable to different atomic environments and provide results that agree well with those of all-electron calculations[8,25].

The norm-conserving pseudopotentials[16,19] use angular momentum projectors to force pseudo wavefunctions to agree exactly with atomic all-electron wavefunctions beyond a matching radius, typically chosen slightly beyond the core radius. A Kleinman-Bylander form of pseudopotentials[26] converts the angular projectors to limited-range 3D projectors, significantly simplifying their applications in calculations that use plane-wave basis sets. Ultrasoft pseudopotentials[17] relax the norm-conservation criteria and further reduce the basis set size but introduce sharp augmented charge densities near the atomic cores that require careful numerical treatment. Recently, Hamann[19] incorporated the main aspects of ultrasoft pseudopotentials into a norm-conserving form and generated pseudopotentials with multiple projectors for each angular momentum. As a result, these pseudopotentials are nearly as soft as the ultrasoft ones while avoiding the complexity of the augmented charge density.

In the last few decades, considerable work has been devoted to developing methods for solving the Kohn-Sham equations using pseudopotentials. The wave functions are usually expanded in a basis set, and the resulting secular equations are solved using matrix methods, which provide wave function information used to analyze physical phenomena. Many physics-, chemistry- or mathematics-motivated bases exist, including plane waves[27–33], atomic or atomic-like orbitals[34–37], Gaussians[38–45], real-space grids[46–61], wavelets[62–65], and finite elements[66–68].

The most widely used approaches use plane waves as a basis, taking advantage of the fact that the kinetic energy operator is diagonal in Fourier space, while the potential is diagonal in real space (except for the non-local projectors and non-local exchange). The transformations between the two spaces use Fast Fourier Transforms (FFTs), which have the well-known *MlogM* scaling with the number of plane waves or grid points. Another advantage of plane-wave calculations is using a single, easy-to-understand parameter determining the basis set size and thus the computational precision: the highest kinetic energy of plane waves included in the calculations – the plane-wave cutoff.

Since real space is the dual to Fourier space, methods using uniformly-spaced grids[46–50,53–61] should offer similar advantages to plane waves and avoid extensive use of FFTs, the price being an inexact treatment of the kinetic energy operator. As shown in the sections below, adaptive discretization of this operator leads to dramatically improved accuracy, facilitating grid-based calculations with modest grid sizes and enabling highly accurate large-scale calculations on modern parallel computers.

The rest of the paper is organized as follows. We first present an analysis of the finite difference operator in the context of electronic structure calculations, followed by a procedure to generate standard finite difference operators for non-orthogonal lattices. Next, we introduce an adaptive finite difference operator optimized for electronic structure calculations and present the results of the Δ test, a well-known test[8] evaluating the accuracy of electronic structure codes, comparing grid-based results to highly accurate all-electron benchmarks for 71 elements. The following subsections examine energy convergence with grid spacing, and show an example of a highly accurate, large-scale DFT calculation obtained using the adaptive operator, parallelized over the hundreds of CPU-GPU nodes of an exascale supercomputer. All the grid-based calculations use the Real-space MultiGrid (RMG) code[48,49,69].

RESULTS

Analysis of the finite difference operator

Real-space, grid-based methods for solving the Kohn-Sham equations typically use finite differences (FD) to implement the kinetic energy operator $-\nabla^2$ appearing in the Kohn-Sham equation. The space locality inherent to FD operators is computationally efficient and suitable for parallelization via domain decomposition, which partitions the computational volume into subvolumes assigned to different nodes. In plane-wave methods, the Laplacian operator is trivial, while the charge density calculations and applications of the potential need transferring of all the wave functions from the plane wave representation to real space using Fast Fourier Transforms (FFTs), which require communications across the entire computational domain. However, the plane-wave treatment of the Laplacian is exact within the basis set defined by the G-space cutoff, while the FD approximation introduces errors. Minimizing the FD error is thus necessary to exploit the computational advantages possible in real space. The various approaches have included non-uniform grids[46], higher-order central finite difference operators[47,70], the Mehrstellen discretization in our previous version of the RMG package[48,49], and adaptive coordinates and grids[51,71].

We begin the analysis by considering the standard central finite difference approximation for the second derivative of a function $f(x)$ on a uniform grid of spacing h, using $2n+1$ grid points, as given by Eq. (2).

The coefficients a_i are chosen to make the expression exact for polynomials of degree less than or equal to $2n$

$$f_n''(x_0) = a_0 f(x_0) + \sum_{i=1}^{n} a_i (f(x_0 + ih) + f(x_0 - ih)) + R_n\left(h^{2n}\right), \quad (2)$$

where the truncation error is

$$R_n = b_n h^{2n} f^{2n+2}(x_0) + O\left(h^{2n+2}\right) \quad (3)$$

and the b_n arise from the Taylor series expansions used to derive Eq. (2), with $b_1 = \frac{1}{12}, b_2 = \frac{1}{24}$ etc. There are alternate representations of the Laplacian where the coefficients are optimized for a different set of properties. For example, controlling dispersion is required for stable finite difference solutions to the wave equation, and there is a large body of work on this specific topic[72–74]. The goal is to find coefficients for use in Eq. (2) that are optimized for electronic structure calculations. Let $f(x)$ be represented by a plane wave expansion of the form below

$$f(x) = \sum_{j=1,N} C_j \exp\left(iG_j x\right). \quad (4)$$

The first term of the truncation error in Fourier space can be written as

$$R_n = b_n h^{2n} \sum_{j=1,N} \left(iG_j\right)^{2n+2} C_j \exp\left(iG_j x_0\right). \quad (5)$$

For each frequency, the truncation errors of different orders are proportional to the $C_j's$, which are determined by the Fourier transform of the original function. Therefore, a linear combination of finite difference operators of different orders can be constructed to reduce the truncation error. The adaptive operator

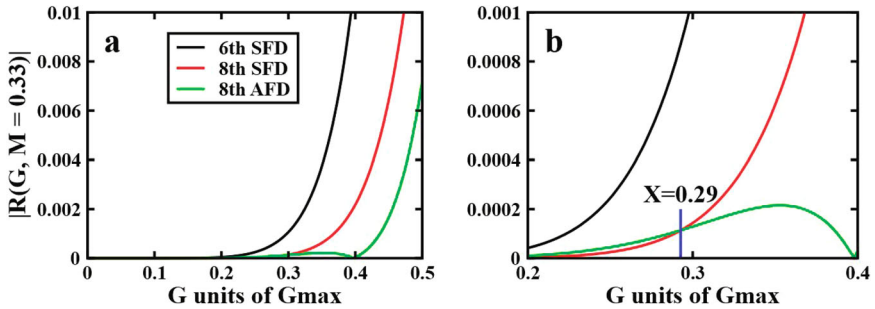

Fig. 1 Truncation errors in finite difference operators. a, **b** Absolute value of the finite difference truncation error of plane waves with different G vectors, up to half of the Nyquist frequency G_{max}. The 8th-order AFD operator uses a mixing value of $M = 0.33$. Part **b** is an enlargement of the low-G part of **a**. The vertical axes units are $1/h^2$ (see Eq. 7).

can be written as

$$f''_{\{new\}}(x_0) = (1+M)f''_n(x_0) - Mf''_{n-1}(x_0). \tag{6}$$

The composite operator is guaranteed to be exact for polynomials up to degree $2(n-1)$, while a further variation of M may be used to minimize the truncation error for a target class of functions. This method of optimizing finite difference operators by mixing stencils of a different order is not necessarily appropriate for arbitrary functions but has been used successfully for specific purposes[74]. In our RMG implementation and tests, we found that M is always positive. This is supported by the error analysis below.

Analyzing the error in more detail is useful when the adaptive operator is applied to plane waves. For a given reciprocal vector G, the truncation errors for a standard nth order operator can be expressed as a power series

$$R_n^s(G) = \frac{1}{h^2}\sum_{m=1,2\ldots} b_{n,m}(ihG)^{2n+2m} \tag{7}$$

Here we ignore the phase term e^{iGx_0}. For a periodic system, the values of hG are always in the range of [-π,π]. The $b_{n,m}$ decrease with increasing m, and the signs of the errors alternate for m = even or odd, but the errors for hG≫1 are still large compared to the small hG range.

The truncation error for the adaptive nth order operator is

$$R_n^a(G,M) = (1+M)R_n^s(G) - MR_{n-1}^s(G) \tag{8}$$

For a given n, the constants $b_{n,m}$ may be evaluated using a symbolic math package (e.g., SymPy[75]). For the 8th order adaptive operator ($n = 4$) we obtain the truncation error

$$R_4^a(G,M) = \frac{1}{h^2}\left[-\frac{M}{560}(hG)^8 + \left[\frac{1}{3156}+\frac{M}{1680}\right](hG)^{10} - \left[\frac{1}{13860}+\frac{19M}{201600}\right](hG)^{12} + \ldots\right] \tag{9}$$

Figure 1 is a graph of the truncation error vs. G from Eq. 9 for $M = 0.33$ as well as graphs of the errors for the 6th and 8th order standard operators used to construct the adaptive. It's clear from the graph and Eq. 7 that the error increases rapidly as hG → 1. Therefore, a necessary condition for using finite differences in electronic structure calculations is for the wavefunction components to be small when |hG|>1 and approach zero as |hG| is close to its maximum π. Fig. 1a shows that for G>X ≅ 0.29 the adaptive operator is more accurate than the standard 8th while the zoomed view in Fig. 1b shows that for G<X the standard 8th order is slightly more accurate. The absolute magnitude of the errors is very different in the two regions, with the adaptive operator having a significantly flatter error curve over a broader range than the standard operators. The total truncation error depends on *both* $R_a^n(G,M)$ and the profile of $\psi(G)$, with the adaptive process optimizing M to minimize the total error. However, the calculations presented later show that even a fixed value of $M = 0.33$ leads to more accurate results for a wide range of atomic species and grid spacings. While the reason for this is not immediately obvious, it can be understood by focusing on the differential absolute errors in the regions to the left and right of $G = X$ in Fig. 1. The absolute errors for plane waves with $G<X$ are small for both adaptive and standard operators. In a high-cutoff calculation, where the wavefunctions have little weight for $G>X$, the overall error and the differences between the operators are small. For a less converged calculation, where the wavefunctions have significant components for $G>X$, the adaptive operator has a significantly lower total error because the errors for the standard operators increase rapidly in this region. As noted earlier, the 8th-order adaptive operator with $M = 0.33$ performs well over a wide range of atomic species and grid spacings, but as the grid density becomes very high, there is a point where the standard operators are more accurate because the wavefunctions have vanishing components for $G>X$. The fully adaptive operator overcomes this issue by optimizing M for specific calculations, decreasing M as the convergence level increases.

Finite difference operator by Taylor Series expansion

For cubic or orthorhombic lattice systems, the lattice vectors are orthogonal to each other, and the FD operators can be obtained separately for each direction. For a general lattice type, where the lattice vectors are not orthogonal, such as monoclinic or triclinic systems, the following process is used to generate the initial coefficients for a specific order. Then, the procedure discussed in the next subsection is used to optimize the FD operator further to reach high precision without increasing the computational cost.

First, a few special axes in the real-space grid are chosen appropriately for the lattice type; axes that coincide with the lattice vectors are always included. $2n$ grid points along each axis are used for the following minimization. For each point, the function f(x,y,z) can be expressed as the Taylor series expansion

$$f\left(x_i,y_j,z_k\right) = f(x_0,y_0,z_0) + \sum_{lmp}\frac{f^{(lmp)}}{l!\,m!\,p!}h_x^l h_y^m h_z^p + \delta(ijk) \tag{10}$$

Where f^{lmn} are the derivatives to be determined and $l+m+p < 2n+1$ for the 2n-order FD operator. We define an error norm R by

$$R = \sum_{ijk}\frac{|\delta(ijk)|^2}{h_{ijk}^3} \tag{11}$$

where $\delta(ijk)$ is defined in Eq. (10) and h_{ijk} is the distance from the point (x_i,y_j,z_k) to the point (x_0,y_0,z_0).The summation is over the set {ijk} of points included in the FD operator. For monoclinic or triclinic systems, the sampling grid points are on axes along the lattice vectors and also additional axes. The FD coefficients can be

obtained by minimizing the norm in Eq. 11, and we have

$$\frac{\partial R}{\partial f^{(lmp)}} = 0 \tag{12}$$

This will generate a set of linear equations and the derivatives $f^{(lmp)}$ can be obtained by solving these linear equations[76]. One can always avoid the singularity of the linear equations by including more grid points and axes.

For orthogonal lattices, the resulting FD kinetic energy operator is separable. For non-orthogonal lattices, cross terms occur, but both the kinetic energy operator and the first derivatives are obtained from the same sampling points with predetermined coefficients. Recently, a Kronecker product formulation of the kinetic energy operator for non-orthogonal lattices has been developed[77]. All of the derivatives are applied separately on the lattice vectors, but the cross terms $\partial^2/\partial\zeta\partial\eta$ need to be applied sequentially on each lattice vector. We have not explored this formulation.

Adaptive finite difference operator

A generalization from the one-dimensional mixed operator case discussed above to three dimensions is trivial, i.e., the truncation error in one lattice frequency is always proportional to the component of the target function at that frequency. This is true for all lattice types in solid-state physics, and the operators along the different axes are determined by the method described above.

For electronic structure applications in which the Kohn-Sham equation is solved numerically, the target functions are the Kohn-Sham wave functions. To a first-order approximation, these may be written as a linear combination of the pseudo atomic orbitals ψ_{atomic}. In a non-atomic environment, the ψ_{atomic} should still provide a good representation of the Kohn-Sham wave functions in the regions near the ionic cores, as is implicitly assumed in the linear combination of atomic orbitals (LCAO) methods for calculating the electronic structure of molecules and solids[78]. In the interstitial regions, their deviation from the pseudo atomic orbitals may be larger, but as they are much less rapidly varying than in the core regions, an operator of the above form, which is exact for polynomials of degree $2(n-1)$, is highly accurate for a sufficiently large n. For these reasons, the pseudo atomic orbitals were chosen as the optimization functions for the finite difference operators. In analogy with pseudopotentials, operators constructed using this procedure are highly accurate for isolated atoms and should also be transferrable to solids or molecules.

The optimization procedure requires a reference standard. For a function discretized on a uniform real space grid, the most accurate Laplacian operator is the FFT method. Unfortunately, this would require transforming all the real-space wave functions to the reciprocal space via FFTs. For very large calculations in which the wave functions are distributed across many computing nodes, the FFTs are too slow because they require global communications. Nevertheless, the FFT Laplacian is well-suited as a reference standard because it only needs to be computed once for each atomic orbital. The overall computational cost is negligible. We choose the objective function to be minimized as the norm of the difference between the kinetic energies of the real-space atomic orbitals computed via FFT versus their values computed by finite differences. Weighting factors are applied based on the atomic orbital occupations and the number of atoms of each kind in the anticipated large calculation. The final formula is

$$F(M) = \sum_{i=1,N} w_i |<\psi_i(r)|L_{FD}(M) - L_{FFT}|\psi_i>|^2, \tag{13}$$

where ψ_i is one of the distinct atomic orbitals, and w_i is the weight factor equal to the total occupancy for this orbital. L_{FD} is the finite differential Laplacian operator and L_{FFT} is the FFT Laplacian operator. The minimization process for $F(M)$ can be performed by using a least-squares fit of the resulting data to determine the minima. If the deviation is too large for any orbital of a specie included in the calculations than a given tolerance, which we set at 10^{-4}, the grid spacing is decreased. If desired, this procedure can be automated.

Figure 2a, b show the Ni $3d_{xz}$ orbital in real and G spaces, respectively. Although the truncation errors for the high-frequency plane waves are large, the orbitals have very small components in this range, which can be clearly seen in Fig. 2b. Figures 2c and d show the truncation errors in real and G spaces for this orbital with different finite-difference operators. As was noted before, the truncation error at a specific G vector is proportional to the orbital's component at this frequency. This can be clearly seen in Fig. 2d, where the errors have the same trends for both 6th- and 8th-order standard FD operators, independent of the grid spacings or the effective cutoff energies. In real space, the errors also have the same trends for both 6th- and 8th-order SFDs. Therefore, the errors are dramatically reduced with the adaptive 8th-order FD operator. In fact, it has better accuracy than the standard 12th-order FD operator (see below). The optimization uses the atomic orbitals as the target functions, and the resulting AFD is transferable to the wavefunctions in the real applications. Figure 2e and f shows the finite-difference errors (compared to the FFT results) for the highest occupied molecular orbital (HOMO) and the lowest unoccupied molecular orbital (LUMO) of NiO in a 64-atom cell. In the interstitial regions, the wavefunctions are smooth, and the errors from both SFD and AFD are small. In the regions near atoms, the errors from AFD are significantly smaller than those from SFD. This indicates that AFD is more accurate than SFD not only for the atomic orbitals but also for the extended-state wave functions. The more accurate total energy in the next section also proves that. Since a high-order FD operator requires more computational resources than the lower-order one, not only because of the size of the FD tensor but also the communication cost of reaching adjacent domains when domain decomposition is used in massively parallel calculations, the adaptive finite difference (AFD) operator leads to more accurate results at a significantly lower computational cost. We discuss the computational advantages of AFD below.

Accuracy across the periodic table

The DFT Δ test[8,79] was selected to test the adaptive operators in the RMG code[80] across a wide range of atomic species and lattice types. The Δ test evaluates the average variance between the equations of state calculated by different codes and has become a standard way of comparing the computational accuracy and reproducibility of DFT codes using different all-electron or pseudopotential methods, basis sets, and algorithms for 71 different atomic species. Published results listing the average Δ are available[81] for a large selection of DFT codes, using highly-converged all-electron results obtained by the WIEN2k code[82] as the reference standard. For comparisons with other codes, we used a mixture of ONCV, GBRV, and pslibrary pseudopotentials that tracked closely with the SSSP accuracy library[83], for which exhaustive tests of transferability and accuracy have been carried out[83]. The correspondence was not exact, as RMG does not support PAW-based pseudopotentials used for some atomic species in the SSSP library. Instead of PAW-based potentials, we used those from the SG15[84] or the GBRV[85] libraries. The developers of these and other libraries chose to include semi-core orbitals for many elements for reliability, transferability, and precision, see Supplementary Table 1. The authors are not pseudopotential developers and had no role in choosing the semi-core configurations. In general, the pseudopotential developers include semicore electrons in the calculations if they have significant spatial overlap with valence electrons and thus affect interatomic interactions, as uncovered by extensive testing. As an

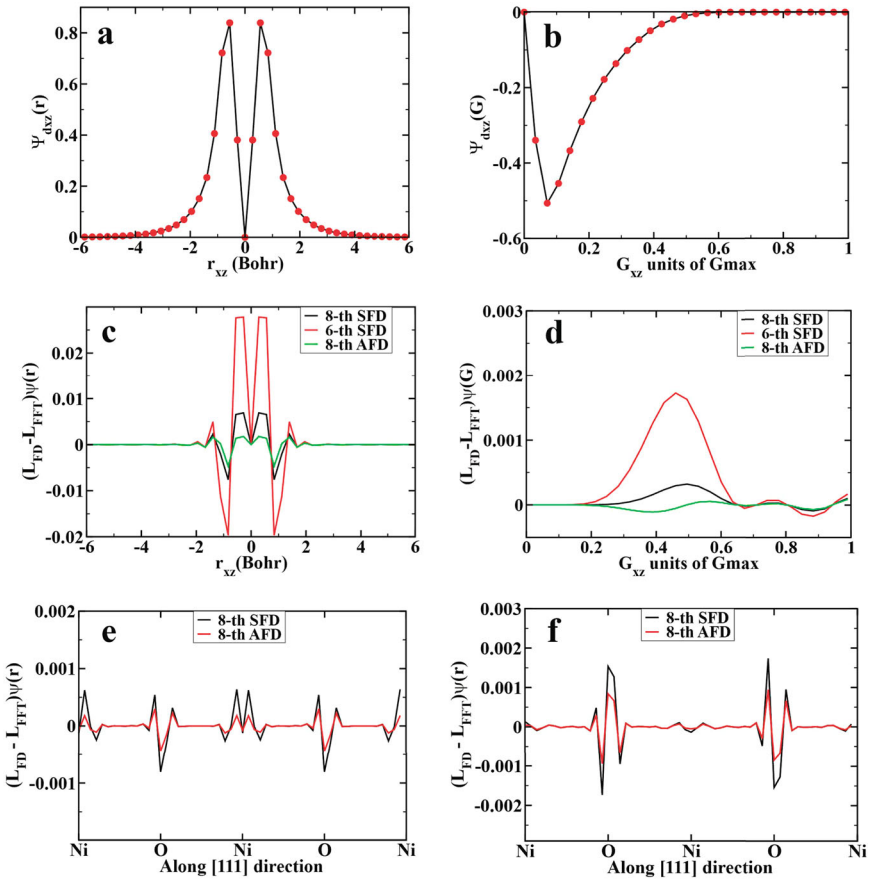

Fig. 2 Orbital and discretization errors in real space and reciprocal G space. Ni $3d_{xz}$ orbital in (**a**) real space and (**b**) G space, along the xz direction. Finite difference errors of Ni $3d_{xz}$ orbital in **c** real space and **d** G space, along the xz direction. Finite difference errors for **e** HOMO and **f** LUMO wave functions of NiO along the [111] direction. Ni-O distance is 3.61 Å. The atomic orbitals in both real and G spaces and the wavefunctions (in real space) are all normalized to unity.

example, consider the 5th column atoms As, Sb, and Bi. For the 4th row As, the pseudopotential only includes 4 s and 4p electrons. For the 5th row Sb, the pseudopotential includes the semicore 4d electrons in addition to 5 s and 5p. For the large-core 6th row Bi, the SSSP accuracy pseudopotential includes the semicore 5 s, 5p, and 5d electrons, in addition to 6 s and 6p. One should note that the Δ-test grid spacings for As, Sb, and Bi are similar, 0.236–0.281 bohr.

Figure 3 provides an element-by-element comparison of the individual Δ values for the 8th-order adaptive and the 12th-order standard finite difference operators at the same grid spacings. The 3 largest Δ values for the standard 12th-order operator are for Fe, Co, and Lu. They represent elements with extremely hard pseudopotentials and highly localized orbitals. Removing all of them from averaging produces an average value of 0.503 meV, which is 69% worse than the value of 0.298 meV for the adaptive 8th-order operator. Table 1 lists the average Δ values for the 8th, 10th and 12th- order standard operators as well as the 8th-order adaptive and 8th-, 10th-and 12th-order operators with fixed mixing. The latter are generated using the same mixing value for all species, making them easy to implement. They produce lower Δ values than the standard operators of the same order, although not as low as the fully adaptive 8th. One should note that the total energy must converge to the same value when the grid spacing is small enough for both standard and adaptive operators. This can be seen in Fig. 4 described in the next subsection. In all the cases shown there, the total energy converges to the same value at an extremely high cutoff energy (corresponding to a very small grid spacing), but the 8th-order AFD converges much faster than the

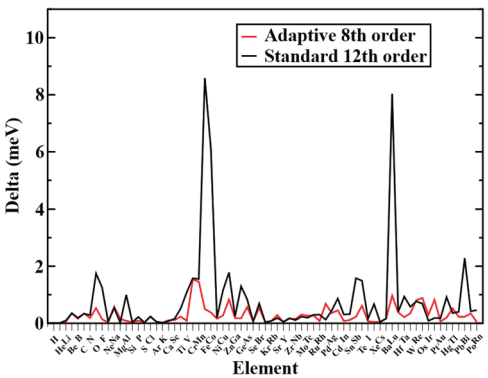

Fig. 3 Δ value comparison for the 8th order adaptive and 12th order standard operators. The results were obtained using RMG version 5.3.

higher-order SFDs, and reaches plane-wave precision at a similar effective cutoff as plane waves.

Energy convergence with the grid spacing

In this subsection, we examine the convergence of the total energy versus grid resolution, represented by the corresponding plane-wave kinetic energy cutoff, of various forms of finite-differencing of the kinetic energy, compared to a reference value obtained by a plane-wave code that treats the kinetic energy exactly at that cutoff. For a given grid (N_1,N_2,N_3) in real space,

where $N_{1,2,3}$ are the numbers of grid points along the three lattice vectors, the corresponding grid in the reciprocal space (FFT grid) has the same dimensions along the three reciprocal lattice vectors. All the grid points in the reciprocal space can be written as $\boldsymbol{G_{ijk}} = i\boldsymbol{b_1} + j\boldsymbol{b_2} + k\boldsymbol{b_3}$ where $\boldsymbol{b_{1,2,3}}$ are the reciprocal lattice vectors and $-\frac{1}{2}N_{1,2,3} \leq i, j, k \leq \frac{1}{2}N_{1,2,3}$. These **G** vectors form a hexahedron, and we compute the kinetic energy cutoff as the radius squared of the inscribed sphere of this hexahedron, which is consistent with the procedures used by plane wave codes. For cubic or orthorhombic lattices with a single grid spacing, the conversion factor between the grid spacing h and the kinetic energy cutoff becomes $(\pi/h)^2$ (Ry). While the Δ test consists of calculations for elemental solids, we use supercells with more than one type of atom here, employing norm-conserving pseudopotentials (NCPP)[16,19]. While the AFD method is equally applicable to ultrasoft pseudopotentials (USPP)[17], the wavefunctions from NCPP are typically more rapidly varying than those from USPP and therefore provide a more rigorous test of the quality of the operator. The reported results were generated using the SG15 potentials developed by Schlipf and Gygi[84] using Hamann's ONCV code[19,86]. The first system is the Mott insulator NiO, represented by a 64-atom supercell of NiO in an antiferromagnetic configuration, with Ni $3s^2 3p^6$ semi-core states included in valence. Figure 4a shows the difference in total energy ΔE between a reference value and RMG v.5.3 using various forms of the kinetic energy operator. The reference values were generated using the open-source plane-wave code Quantum Espresso (QE)[31,87] that has an exact representation of the operator within its basis set. While all of the finite-difference-based operators achieve good agreement with QE at high energy cutoffs, the adaptive operators are considerably more accurate at lower cutoffs. Indeed, the 8th-order AFD operator is more accurate than the 12th-order standard operator up to a 205 Rydberg cutoff, with the difference at 124 Rydbergs being a factor of 11.

Table 1. Average delta values for various finite difference methods.

Finite difference method	Δ value (meV)
8th order standard	3.753
10th order standard	1.540
12th order standard	0.802
8th order fixed (M = 0.33)	1.241
10th order fixed (M = 0.416)	0.553
12th order fixed (M = 0.5)	0.486
8th order adaptive	0.298

The second test case is borax decahydrate, $Na_2[B_4O_5(OH)_4]\cdot 8H_2O$, which has a complex monoclinic structure with 86 atoms in the primitive cell and a mixture of covalent, ionic, and hydrogen bonds[88]. As shown in Fig. 4b, the adaptive finite differencing is more accurate than the standard 10th- and 12th-order finite-difference formulas at all tested cutoffs, with the difference exceeding a factor of 200 at 117 Rydbergs, and converges more quickly to the reference value.

Figure 4c shows the time per SCF step at a prescribed precision for borax decahydrate, compared to the reference Quantum Espresso plane wave calculation. For the same precision, the standard finite difference operators require significantly denser grids than the adaptive operator, and thus their times per SCF step are substantially greater.

Large-scale DFT calculations using the adaptive operator

The adaptive finite-difference operator enables high-accuracy calculations for large systems at significantly reduced cost. As an example, we consider a 2,016-atom NiO cell in an antiferromagnetic configuration, also with Ni $3s^2 3p^6$ semi-core states included in valence. The calculation was spin-polarized and used 14,128 Kohn-Sham wavefunctions for each spin channel. Based on the convergence versus grid spacing results in the left panel of Fig. 2, a grid spacing corresponding to an energy cutoff of 167 Ry was selected for the adaptive operator. For the standard finite difference operator, similar accuracy in this cell requires the substantially larger cutoff of 254 Ry. The results were obtained using the exascale Frontier supercomputer at ORNL. Each node contains a 64-core AMD Epyc 7453 CPU and four AMD MI250X GPUs. The RMG calculations used all CPU cores and all GPUs in each node. The scaling results for 18 to 144 nodes are presented in Fig. 5. For the AFD calculations, a minimum of 18 nodes is required due to their memory footprint. The SFD calculations require a significantly higher grid density for comparable precision and do not fit into 18 nodes. The SFD results are thus presented for 36 to 144 nodes.

Figure 5 clearly demonstrates the advantages of AFD, both in terms of computational time and the required memory. On 36 nodes, AFD calculations are more than twice as fast as the SFD ones. This ratio decreases somewhat for larger numbers of nodes because the grid operations count per node becomes smaller and does not fully saturate the computational capacity of each node. It should be noted that AFD calculations are practical already on 18 nodes, as the time per SCF step, 230 seconds, makes high-accuracy calculations of this size feasible even when the problem requires extensive geometry optimizations, transition path studies, or ab initio molecular dynamics.

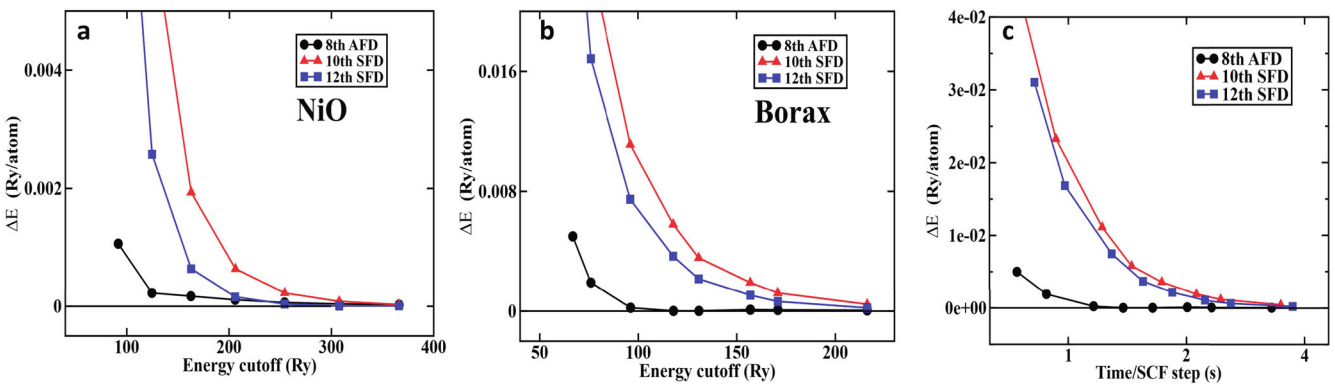

Fig. 4 Differences in total energies between the reference energy obtained using Quantum Espresso and RMG, and timings. a a 64-atom NiO cell in an antiferromagnetic configuration, and **b** an 86-atom borax decahydrate $Na_2[B_4O_5(OH)_4]\cdot 8H_2O$ cell, as functions of plane-wave kinetic energy cutoff; **c** time per SCF step for grid densities required to reach prescribed accuracies in comparison to the reference energy.

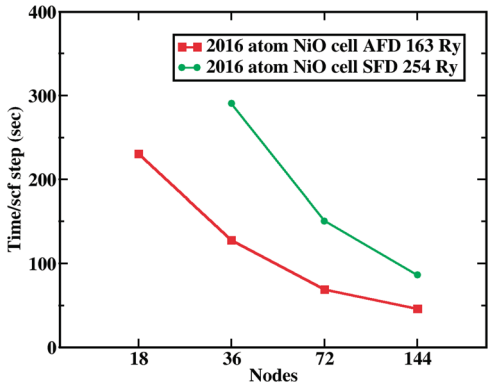

Fig. 5 Scaling of the 2,016-atom NiO high-accuracy calculations with adaptive (AFD) and standard (SFD) finite difference operators with the number of Frontier nodes. The standard operator requires a significantly larger grid density for equivalent accuracy. See text.

DISCUSSION

The promise of real-space electronic structure calculations has always centered on their easy parallelizability on massively parallel computer architectures through domain decomposition, because real-space operations are inherently local and thus amenable to parallel execution without extensive communication. However, for grid-based calculations, it is well-established that high-order discretization of the kinetic energy operator is required, which makes the calculations more costly and less local by increasing the communications beyond the local domain. In contrast, plane-wave calculations represent the kinetic energy operator exactly for a given cutoff but require global fast Fourier transform operations. The adaptive finite-differencing scheme developed in this paper relies on optimizing the kinetic energy expression near atomic cores for each atomic specie separately, resulting in finite-difference coefficients that are transferable to different atomic environments in analogy with pseudopotentials, which both grid- and plane-wave-based methods use. The resulting adaptive kinetic energy operator is far more accurate than standard high-order discretizations and lower-order, decreasing the costs of both calculations and communications. We have tested the accuracy of this operator in electronic structure calculations using the well-known Δ test for 71 elemental solids, and the average error of the calculations was the same as those of the well-established plane-wave codes VASP and Quantum Espresso. The accuracy of the adaptive operator was further established with multi-specie tests on NiO and borax decahydrate, which exhibit a range of complex bonding arrangements. The scalability of real-space grid methodology was then confirmed in highly accurate calculations for a 2,016-atom NiO supercell.

METHODS

Density functional theory calculations

The adaptive finite difference operator for the kinetic energy was implemented in version 5 of the open-source RMG code for all crystallographic space groups. The calculations for the Mott insulator NiO used the DFT + U formalism[89] with PBE exchange-correlation functional[90] and U = 6.5 eV. Due to supercell sizes, only Γ point sampling was used. The calculations for borax decahydrate used the PBE functional and were also at Γ. The Δ test calculations used structures provided at https://molmod.ugent.be/sites/default/files/Delta_v3-1_0.zip with varying k-point meshes depending on the specific element. All input and output data are available from the depository listed below.

DATA AVAILABILITY

All input and output files used to report the results and create the graphics are available at https://doi.org/10.17605/OSF.IO/3S4VK.

CODE AVAILABILITY

The open-source RMG code is distributed through github.com/RMGDFT.

Received: 2 March 2023; Accepted: 9 January 2024;
Published online: 20 January 2024

REFERENCES

1. Hohenberg, P. & Kohn, W. Inhomogeneous electron gas. *Phys. Rev.* **136**, B864–B871 (1964).
2. Kohn, W. & Sham, L. J. Self-consistent equations including exchange and correlation effects. *Phys. Rev.* **140**, A1133–A1138 (1965).
3. Dreizler, R. M. & Gross, E. K. U. *Density functional theory: an approach to the quantum many-body problem*. (Springer-Verlag), (1990).
4. Jain, A. et al. Commentary: The Materials Project: A materials genome approach to accelerating materials innovation. *APL Mater.* **1**, 011002 (2013).
5. Curtarolo, S. et al. AFLOW: An automatic framework for high-throughput materials discovery. *Comput. Mater. Sci.* **58**, 218–226 (2012).
6. Talirz, L. et al. Materials Cloud, a platform for open computational science. *Sci. Data* **7**, 299 (2020).
7. Sbailò, L., Fekete, Á., Ghiringhelli, L. M. & Scheffler, M. The NOMAD Artificial-Intelligence Toolkit: turning materials-science data into knowledge and understanding. *Npj Comput. Mater.* **8**, 1–7 (2022).
8. Lejaeghere, K. et al. Reproducibility in density functional theory calculations of solids. *Science* **351**, aad3000 (2016).
9. Perdew, J. P. & Schmidt, K. Jacob's ladder of density functional approximations for the exchange-correlation energy. *AIP Conf. Proc.* **577**, 1–20 (2001).
10. Becke, A. D. A new mixing of Hartree–Fock and local density-functional theories. *J. Chem. Phys.* **98**, 1372–1377 (1993).
11. Heyd, J., Scuseria, G. E. & Ernzerhof, M. Hybrid functionals based on a screened Coulomb potential. *J. Chem. Phys.* **118**, 8207–8215 (2003).
12. Chai, J.-D. & Head-Gordon, M. Systematic optimization of long-range corrected hybrid density functionals. *J. Chem. Phys.* **128**, 084106 (2008).
13. Wimmer, E., Krakauer, H., Weinert, M. & Freeman, A. J. Full-potential self-consistent linearized-augmented-plane-wave method for calculating the electronic structure of molecules and surfaces: O2 molecule. *Phys. Rev. B* **24**, 864–875 (1981).
14. Blaha, P., Schwarz, K., Sorantin, P. & Trickey, S. B. Full-potential, linearized augmented plane wave programs for crystalline systems. *Comput. Phys. Commun.* **59**, 399–415 (1990).
15. Methfessel, M., Rodriguez, C. O. & Andersen, O. K. Fast full-potential calculations with a converged basis of atom-centered linear muffin-tin orbitals: Structural and dynamic properties of silicon. *Phys. Rev. B* **40**, 2009–2012 (1989).
16. Hamann, D. R., Schlüter, M. & Chiang, C. Norm-conserving pseudopotentials. *Phys. Rev. Lett.* **43**, 1494 (1979).
17. Vanderbilt, D. Soft self-consistent pseudopotentials in a generalized eigenvalue formalism. *Phys. Rev. B* **41**, 7892 (1990).
18. Blöchl, P. E. Projector augmented-wave method. *Phys. Rev. B* **50**, 17953–17979 (1994).
19. Hamann, D. R. Optimized norm-conserving Vanderbilt pseudopotentials. *Phys. Rev. B* **88**, 085117 (2013).
20. Kahn, L. R., Baybutt, P. & Truhlar, D. G. Ab initio effective core potentials: Reduction of all-electron molecular structure calculations to calculations involving only valence electrons. *J. Chem. Phys.* **65**, 3826–3853 (1976).
21. Hay, P. J., Wadt, W. R. & Kahn, L. R. Ab initio effective core potentials for molecular calculations. II. All-electron comparisons and modifications of the procedure. *J. Chem. Phys.* **68**, 3059–3066 (1978).
22. Hay, P. J. & Wadt, W. R. Ab initio effective core potentials for molecular calculations. Potentials for the transition metal atoms Sc to Hg. *J. Chem. Phys.* **82**, 270–283 (1985).
23. Gygi, F. All-electron plane-wave electronic structure calculations. *J. Chem. Theory Comput.* **19**, 1300–1309 (2023).
24. Kleinman, L. Relativistic norm-conserving pseudopotential. *Phys. Rev. B* **21**, 2630–2631 (1980).
25. Borlido, P., Doumont, J., Tran, F., Marques, M. A. L. & Botti, S. Validation of pseudopotential calculations for the electronic band gap of solids. *J. Chem. Theory Comput.* **16**, 3620–3627 (2020).

26. Kleinman, L. & Bylander, D. M. Efficacious form for model pseudopotentials. *Phys. Rev. Lett.* **48**, 1425–1428 (1982).
27. Kresse, G. & Furthmüller, J. Efficiency of ab-initio total energy calculations for metals and semiconductors using a plane-wave basis set. *Comput. Mater. Sci.* **6**, 15–50 (1996).
28. Kresse, G. & Joubert, D. From ultrasoft pseudopotentials to the projector augmented-wave method. *Phys. Rev. B* **59**, 1758–1775 (1999).
29. Gonze, X. et al. First-principles computation of material properties: the ABINIT software project. *Comput. Mater. Sci.* **25**, 478–492 (2002).
30. Clark, S. J. et al. First principles methods using CASTEP. *Z. F.ür. Krist. - Cryst. Mater.* **220**, 567–570 (2005).
31. Giannozzi, P. et al. QUANTUM ESPRESSO: a modular and open-source software project for quantum simulations of materials. *J. Phys. Condens. Matter* **21**, 395502 (2009).
32. Gygi, F. Architecture of Qbox: A scalable first-principles molecular dynamics code. *IBM J. Res. Dev.* **52**, 137–144 (2008).
33. Hutter, J., Iannuzzi, M., Schiffmann, F. & VandeVondele, J. cp2k: atomistic simulations of condensed matter systems. *WIREs Comput. Mol. Sci.* **4**, 15–25 (2014).
34. Soler, J. M. et al. The SIESTA method for ab initio order-N materials simulation. *J. Phys. Condens. Matter* **14**, 2745–2779 (2002).
35. Lu, W. C. et al. Molecule intrinsic minimal basis sets. I. Exact resolution of ab initio optimized molecular orbitals in terms of deformed atomic minimal-basis orbitals. *J. Chem. Phys.* **120**, 2629–2637 (2004).
36. Blum, V. et al. Ab initio molecular simulations with numeric atom-centered orbitals. *Comput. Phys. Commun.* **180**, 2175–2196 (2009).
37. Jensen, F. Atomic orbital basis sets. *WIREs Comput. Mol. Sci.* **3**, 273–295 (2013).
38. Boys, S. F. Electronic Wave Functions. I. A General method of calculation for the stationary states of any molecular system. *Proc. R. Soc. Lond. Ser. A* **200**, 542–554 (1950).
39. Gill, P. M. W. Molecular integrals Over Gaussian basis functions. *Adv. Quantum Chem.* **25**, 141–205 (1994).
40. Pople, J. A. & Hehre, W. J. Computation of electron repulsion integrals involving contracted Gaussian Basis functions. *J. Comput. Phys.* **27**, 161–168 (1978).
41. Curtiss, L. A., Raghavachari, K., Redfern, P. C. & Pople, J. A. Assessment of Gaussian-2 and density functional theories for the computation of enthalpies of formation. *J. Chem. Phys.* **106**, 1063–1079 (1997).
42. Gill, P. M. W. & Pople, J. A. The prism algorithm for two-electron integrals. *Int. J. Quantum Chem.* **40**, 753–772 (1991).
43. Frisch, M. J. et al. Gaussian 03, Revision C.02.
44. Schmidt, M. W. et al. General atomic and molecular electronic structure system. *J. Comput. Chem.* **14**, 1347–1363 (1993).
45. Aprà, E. et al. NWChem: Past, present, and future. *J. Chem. Phys.* **152**, 184102 (2020).
46. Bernholc, J., Yi, J. Y. & Sullivan, D. J. Structural transitions in metal-clusters. *Faraday Discuss*. 217–228 (1991).
47. Chelikowsky, J. R., Troullier, N. & Saad, Y. Finite-difference-pseudopotential method: Electronic structure calculations without a basis. *Phys. Rev. Lett.* **72**, 1240–1243 (1994).
48. Briggs, E. L., Sullivan, D. J. & Bernholc, J. Large-scale electronic-structure calculations with multigrid acceleration. *Phys. Rev. B* **52**, R5471–R5474 (1995).
49. Briggs, E. L., Sullivan, D. J. & Bernholc, J. Real-space multigrid-based approach to large-scale electronic structure calculations. *Phys. Rev. B* **54**, 14362–14375 (1996).
50. Seitsonen, A. P., Puska, M. J. & Nieminen, R. M. Real-space electronic-structure calculations: Combination of the finite-difference and conjugate-gradient methods. *Phys. Rev. B* **51**, 14057–14061 (1995).
51. Gygi, F. & Galli, G. Real-space adaptive-coordinate electronic-structure calculations. *Phys. Rev. B* **52**, 2229–2232 (1995).
52. Ono, T. & Hirose, K. Timesaving double-grid method for real-space electronic-structure calculations. *Phys. Rev. Lett.* **82**, 5016–5019 (1999).
53. Mortensen, J. J., Hansen, L. B. & Jacobsen, K. W. Real-space grid implementation of the projector augmented wave method. *Phys. Rev. B* **71**, 035109 (2005).
54. Hodak, M., Wang, S., Lu, W. & Bernholc, J. Implementation of ultrasoft pseudopotentials in large-scale grid-based electronic structure calculations. *Phys. Rev. B Condens. Matter Mater. Phys.* **76**, 085108–085108 (2007).
55. Andrade, X. et al. Real-space grids and the Octopus code as tools for the development of new simulation approaches for electronic systems. *Phys. Chem. Chem. Phys.* **17**, 31371–31396 (2015).
56. Michaud-Rioux, V., Zhang, L. & Guo, H. RESCU: A real space electronic structure method. *J. Comput. Phys.* **307**, 593–613 (2016).
57. Ghosh, S. & Suryanarayana, P. SPARC: Accurate and efficient finite-difference formulation and parallel implementation of Density Functional Theory: Isolated clusters. *Comput. Phys. Commun.* **212**, 189–204 (2017).
58. Ghosh, S. & Suryanarayana, P. SPARC: Accurate and efficient finite-difference formulation and parallel implementation of Density Functional Theory: Extended systems. *Comput. Phys. Commun.* **216**, 109–125 (2017).
59. Xu, Q. et al. Ab initio electronic structure calculations using a real-space Chebyshev-filtered subspace iteration method. *J. Phys. Condens. Matter* **31**, 455901 (2019).
60. Noda, M. et al. SALMON: Scalable ab-initio light–matter simulator for optics and nanoscience. *Comput. Phys. Commun.* **235**, 356–365 (2019).
61. Liou, K.-H., Biller, A., Kronik, L. & Chelikowsky, J. R. Space-filling curves for real-space electronic structure calculations. *J. Chem. Theory Comput.* **17**, 4039–4048 (2021).
62. Harrison, R. J., Fann, G. I., Yanai, T. & Beylkin, G. Multiresolution quantum chemistry in multiwavelet bases. *Lect. Notes Comput. Sci.* 103–110 (2003).
63. Genovese, L. et al. Daubechies wavelets as a basis set for density functional pseudopotential calculations. *J. Chem. Phys.* **129**, 014109–014109 (2008).
64. Yanai, T., Harrison, R. J. & Handy, N. C. Multiresolution quantum chemistry in multiwavelet bases: time-dependent density functional theory with asymptotically corrected potentials in local density and generalized gradient approximations. *Mol. Phys.* **103**, 413–424 (2005).
65. Beylkin, G., Fann, G., Harrison, R. J., Kurcz, C. & Monzón, L. Multiresolution representation of operators with boundary conditions on simple domains. *Appl. Comput. Harmon. Anal.* **33**, 109–139 (2012).
66. Pask, J. E., Klein, B. M., Fong, C. Y. & Sterne, P. A. Real-space local polynomial basis for solid-state electronic-structure calculations: A finite-element approach. *Phys. Rev. B* **59**, 12352–12358 (1999).
67. Motamarri, P., Nowak, M. R., Leiter, K., Knap, J. & Gavini, V. Higher-order adaptive finite-element methods for Kohn–Sham density functional theory. *J. Comput. Phys.* **253**, 308–343 (2013).
68. Das, S., Motamarri, P., Subramanian, V., Rogers, D. M. & Gavini, V. DFT-FE 1.0: A massively parallel hybrid CPU-GPU density functional theory code using finite-element discretization. *Comput. Phys. Commun.* **280**, 108473 (2022).
69. Bernholc, J. et al. Large-scale applications of real-space multigrid methods to surfaces, nanotubes, and quantum transport. *Phys. Status Solidi B* **217**, 685–701 (2000).
70. Wang, J. & Beck, T. L. Efficient real-space solution of the Kohn–Sham equations with multiscale techniques. *J. Chem. Phys.* **112**, 9223–9228 (2000).
71. Waghmare, U. V. et al. HARES: an efficient method for first-principles electronic structure calculations of complex systems. *Comput. Phys. Commun.* **137**, 341–360 (2001).
72. Diaye*, M. N., Hewett, R. J., Atle, A. & Calandra, H. Optimized finite difference coefficients for the Helmholtz equation. in *SEG Technical Program Expanded Abstracts 2015* 3744–3748 (Society of Exploration Geophysicists). https://doi.org/10.1190/segam2015-5827540.1, (2015)
73. Zhang, J.-H. & Yao, Z.-X. Optimized finite-difference operator for broadband seismic wave modeling. *Geophysics* **78**, A13–A18 (2013).
74. Kindelan, M., Moscoso, M. & Gonzalez-Rodriguez, P. Optimized finite difference formulas for accurate high frequency components. *Math. Probl. Eng.* **2016**, e7860618 (2016).
75. SymPy. https://www.sympy.org/en/index.html.
76. Liszka, T. & Orkisz, J. The finite difference method at arbitrary irregular grids and its application in applied mechanics. *Comput. Struct.* **11**, 83–95 (1980).
77. Sharma, A. & Suryanarayana, P. On real-space Density Functional Theory for non-orthogonal crystal systems: Kronecker product formulation of the kinetic energy operator. *Chem. Phys. Lett.* **700**, 156–162 (2018).
78. Slater, J. C. & Koster, G. F. Simplified LCAO method for the periodic potential problem. *Phys. Rev.* **94**, 1498–1524 (1954).
79. Lejaeghere, K., Van Speybroeck, V., Van Oost, G. & Cottenier, S. Error estimates for solid-state density-functional theory predictions: an overview by means of the ground-state elemental crystals. *Crit. Rev. Solid State Mater. Sci.* **39**, 1–24 (2014).
80. *The RMG code* http://www.rmgdft.org/.
81. Comparing Solid State DFT Codes, Basis Sets and Potentials | Center for Molecular Modeling. https://molmod.ugent.be/deltacodesdft.
82. Blaha, P. et al. WIEN2k: An APW+lo program for calculating the properties of solids. *J. Chem. Phys.* **152**, 074101 (2020).
83. Prandini, G., Marrazzo, A., Castelli, I. E., Mounet, N. & Marzari, N. Precision and efficiency in solid-state pseudopotential calculations. *Npj Comput. Mater.* **4**, 1–13 (2018).
84. Schlipf, M. & Gygi, F. Optimization algorithm for the generation of ONCV pseudopotentials. *Comput. Phys. Commun.* **196**, 36–44 (2015).
85. Garrity, K. F., Bennett, J. W., Rabe, K. M. & Vanderbilt, D. Pseudopotentials for high-throughput DFT calculations. *Comput. Mater. Sci.* **81**, 446–452 (2014).
86. Mat-Sim Research. http://www.mat-simresearch.com/.
87. Giannozzi, P. et al. Advanced capabilities for materials modelling with Quantum ESPRESSO. *J. Phys. Condens. Matter* **29**, 465901 (2017).
88. Gainsford, G. J., Kemmitt, T. & Higham, C. Redetermination of the borax structure from laboratory X-ray data at 145 K. *Acta Crystallogr. Sect. E Struct. Rep. Online* **64**, i24–i25 (2008).

89. Anisimov, V. I., Zaanen, J. & Andersen, O. K. Band theory and Mott insulators: Hubbard U instead of Stoner I. *Phys. Rev. B* **44**, 943–954 (1991).
90. Perdew, J. P., Burke, K. & Ernzerhof, M. Generalized gradient approximation made simple. *Phys. Rev. Lett.* **77**, 3865–3868 (1996).

ACKNOWLEDGEMENTS

This research was supported by the U.S. Department of Energy's Exascale Computing Project (ECP), Project Number: 17-SC-20-SC. Computing resources at the Oak Ridge Leadership Computing Facility were provided through the ECP User Program and the Innovative and Novel Computational Impact on Theory and Experiment (INCITE) program.

AUTHOR CONTRIBUTIONS

E.B. and W.L. devised the adaptive operator and performed the calculations. All authors analyzed the results and wrote the manuscript.

COMPETING INTERESTS

The authors declare no competing interests.

ADDITIONAL INFORMATION

Supplementary information The online version contains supplementary material available at https://doi.org/10.1038/s41524-024-01203-y.

Correspondence and requests for materials should be addressed to E. L. Briggs, Wenchang Lu or J. Bernholc.

Reprints and permission information is available at http://www.nature.com/reprints

Publisher's note Springer Nature remains neutral with regard to jurisdictional claims in published maps and institutional affiliations.

Open Access This article is licensed under a Creative Commons Attribution 4.0 International License, which permits use, sharing, adaptation, distribution and reproduction in any medium or format, as long as you give appropriate credit to the original author(s) and the source, provide a link to the Creative Commons license, and indicate if changes were made. The images or other third party material in this article are included in the article's Creative Commons license, unless indicated otherwise in a credit line to the material. If material is not included in the article's Creative Commons license and your intended use is not permitted by statutory regulation or exceeds the permitted use, you will need to obtain permission directly from the copyright holder. To view a copy of this license, visit http://creativecommons.org/licenses/by/4.0/.

© The Author(s) 2024